

Enhancing Quantum Yield in Strained MoS₂ Bilayers by Morphology-Controlled Plasmonic Nanostructures toward Superior Photodetectors

Pavithra Sriram, Yu-Po Wen, Arumugam Manikandan, Kun-Chieh Hsu, Shin-Yi Tang, Bo-Wei Hsu, Yu-Ze Chen, Hao-Wu Lin, Horng-Tay Jeng, Yu-Lun Chueh, and Ta-Jen Yen*



Cite This: *Chem. Mater.* 2020, 32, 2242–2252



Read Online

ACCESS |



Metrics & More

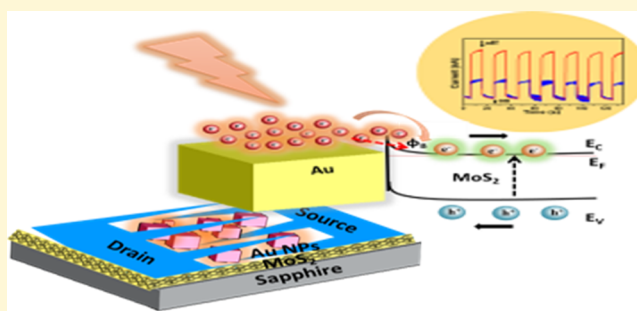


Article Recommendations



Supporting Information

ABSTRACT: Recently, extracting hot electrons from plasmonic nanostructures and utilizing them to enhance the optical quantum yield of two-dimensional transition-metal dichalcogenides (TMDs) have been topics of interest in the field of optoelectronic device applications, such as solar cells, light-emitting diodes, photodetectors, and so on. The coupling of plasmonic nanostructures with nanolayers of TMDs depends on the optical properties of the plasmonic materials, including radiation pattern, resonance strength, and hot electron injection efficiency. Herein, we demonstrate the augmented photodetection of a large-scale, transfer-free bilayer MoS₂ by decorating this TMD with four different morphology-controlled plasmonic nanoparticles. This approach allows engineering the band gap of the bilayer MoS₂ due to localized strain that stems up from plasmonic nanoparticles. In particular, the plasmonic strain blue shifts the band gap of bilayer MoS₂ with 32 times enhanced photoresponse demonstrating immense hot electron injection. Besides, we observed the varied photoresponse of MoS₂ bilayer hybridized with different morphology-controlled plasmonic nanostructures. Although hot electron injection was a substantial factor for photocurrent enhancement in hybrid plasmonic semiconductor devices, our investigations further show that other key factors such as highly directional plasmonic modes, high-aspect-ratio plasmonic nanostructures, and plasmonic strain-induced beneficial band structure modifications were crucial parameters for effective coupling of plasmons with excitons. As a result, our study sheds light on designing highly tailorable plasmonic nanoparticle-integrated transition-metal dichalcogenide-based optoelectronic devices.



INTRODUCTION

Owing to wide-band gap applications, two-dimensional (2D) materials, including graphene and transition-metal dichalcogenides (TMDs), are a fascinating topic in the field of photodetectors, photovoltaics, and electronic transistors.^{1–3} Despite its superior wavelength-range photodetectivity^{4–6} and ultrahigh bandwidth,^{6,7} graphene suffers from limited photoresponsivity due to the vanishing band gap and fleeting carrier lifetime. In contrast, TMDs that promise the potential of achieving very high responsivities are evolving as versatile materials for photodetection applications.^{8–22} For example, MoS₂ monolayers appear as a favorable candidate for photodetectors due to their direct band gap nature^{23,24} and unrivaled transistor behavior.³ However, the low optical cross section of monolayer MoS₂ settles a bottleneck for light–matter interaction and leads to low quantum yield (QY).²⁵

To improve the QY of monolayer MoS₂, plasmonic structures shed light by explicitly coupling the excitons in TMDs and the hot electrons in noble metal nanostructures.²⁶ The decorated metal nanostructures couple with incident light at the surface plasmon frequency, thereby provoking the

localization and enhancement of the electromagnetic field. Moreover, light scattering of metal nanostructures helps increase the optical path length,²⁷ thereby intensifying the light absorption of enclosed semiconductors. In addition, “hot electrons”, which result from the nonradiative decay of plasmons that are injected across the Schottky barrier at the metal–semiconductor interface, enhance the absorbance and Purcell effect.²⁸ Notably, MoS₂ functions as a favorable hot electron acceptor as it has various traps at interfaces^{17,29} (MoS₂/metal, MoS₂/substrate) that trigger internal photogain. Such augmentation of light absorbance paves a promising path for light-harvesting and light-conversion applications.^{30–33}

In this work, we focus on enhancing the photoresponse of large-scale bilayer MoS₂ (about 1 cm²) by coupling the excitons to the properly directed and energetic plasmonic

Received: July 20, 2019

Revised: January 22, 2020

Published: January 22, 2020

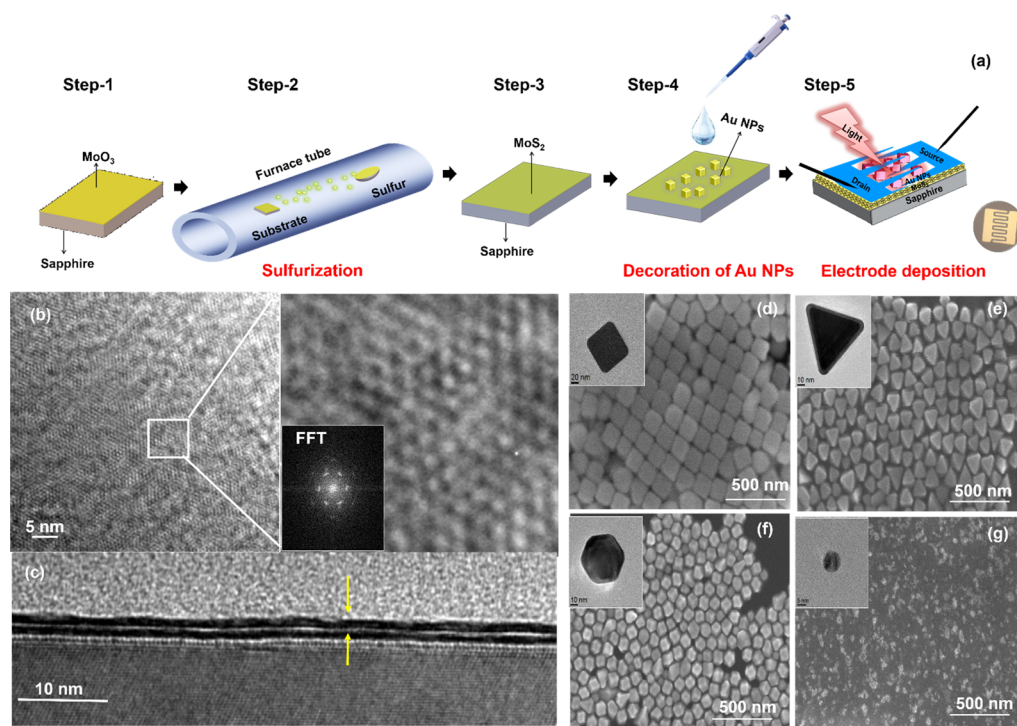


Figure 1. Device fabrication and structural characterization of CVR-grown bilayer MoS₂ and chemically synthesized Au nanostructures. (a) Schematic illustration of the growth process of bilayer MoS₂ on the sapphire substrate, Au nanostructure decoration, and electrode deposition for photodetection. (b) Topological HR-TEM image of bilayer MoS₂ and its magnified image with the FFT image inset. (c) Cross-sectional HR-TEM image of bilayer MoS₂. SEM images of (d) nanocubes, (e) octahedra, (f) rhombic dodecahedra, and (g) nanospheres (TEM images of individual structures are shown in the insets).

mode of morphology-controlled Au nanoparticles along with the localized strain-induced band gap modification. Our studies indicate that the difference in the radiation pattern of plasmonic mode directly influences the coupling of plasmons to the excitons of MoS₂ in their proximity. Meanwhile, the Au nanostructures sitting atop induce local strain in the bilayer MoS₂ film, thereby manipulating its band structure. Together, the overall photoresponsivity of the plasmonically strained hybrid device is significantly enhanced to about $790 \mu\text{A W}^{-1}$, which is 32 times higher than that of the previously reported thermally strained bilayer MoS₂.³⁴ Meanwhile, this hybrid photodetector exhibits a high detectivity of 5.29×10^9 Jones without any gate-induced electric field. This approach allows us to precisely tune the photoresponse of the bilayer MoS₂ film by a prudent selection of nanoparticle morphology simultaneously with strain-induced beneficial band gap modification.

RESULTS AND DISCUSSION

Chemical vapor deposition is typically used to synthesize wafer-scale MoS₂, but it faces the complication of morphology variation over the area of the substrate because of spatially dependent growth parameters.^{22,35} Therefore, in this work, we adopted a two-step sulfurization process called chemical vapor reaction method (CVR)³⁶ for growing a 3 in. wafer-scale and uniform bilayer MoS₂ film. As shown in Figure 1a, first, MoO₃ was deposited on top of a clean sapphire substrate and then followed by a sulfurization process. Next, the sulfur precursors were placed upstream of a gas source near the heating zone of a furnace tube, thereby resulting in MoS₂ bilayer formation on the sapphire substrate. Figure 1b shows the topological high-resolution transmission electron microscopy (HR-TEM) image, which reveals the quality of the CVR-grown bilayer

MoS₂ film, whereas the cross-sectional TEM image in Figure 1c shows the controlled growth of the bilayer MoS₂ film with uniform coverage over the surface. Notably, Figure S1a of the Supporting Information shows the Raman spectrum of bilayer MoS₂ with characteristic peaks of the in-plane Raman mode (E_{2g}^1) and the out-of-plane Raman mode (A_{1g}) at frequencies of 384.2 and 406.4 cm^{-1} , respectively, with a 22.2 cm^{-1} distance between two modes.³⁷

Furthermore, we chemically synthesized a library of morphology-controlled Au nanoparticles, including cubes, octahedra (ODs), rhombic dodecahedra (RDs), and spherical particles by applying seed-mediated and hydrothermal methods (refer to Experimental Methods section for details). The SEM images of these morphology-controlled Au nanostructures with homogeneous distribution are shown in Figure 1d–g (cube, OD, RD, and sphere, respectively), and the TEM image of each individual nanostructure is shown in the corresponding figure insets. In our system, we tailored the size of the nanoparticles to assure the spectral overlap between localized surface plasmon resonances (LSPRs) of Au nanoparticles and the incident excitation wavelength (520 nm), thereby allowing us to govern the excitation enhancement efficiency and quantum yield. Meantime, the excitation wavelength is well above the energy of excitons in MoS₂. Figure S1b presents the ultraviolet–visible (UV–vis) absorption spectrum of Au nanoparticles with four morphologies overlapping with the incident excitation wavelength. The size distribution maps of Au nanoparticles of various shapes are shown in Figure S2 of the Supporting Information. To design the hybrid plasmonic semiconductor device, Au nanoparticles are separately spin-coated at a low rpm onto the MoS₂ bilayer film, as presented in step 4 of Figure 1a. These Au

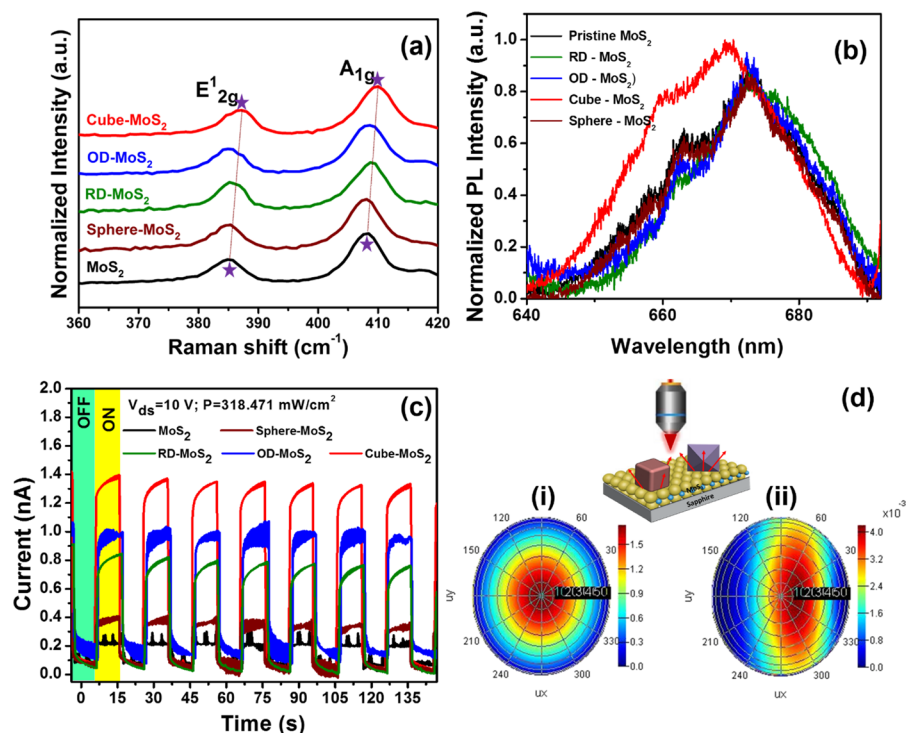


Figure 2. Raman, PL, and photodetector characteristics of Au/MoS₂ hybrids. (a) Raman spectra of bilayer MoS₂ that is decorated with various nanostructures. (b) Normalized PL spectra of bilayer MoS₂ that is decorated with various Au nanostructures. (c) Photocurrent of bilayer MoS₂ that is decorated with various Au nanostructures at an applied bias of 10 V and illuminated by a 520 nm laser with a power density of 318.471 mW/cm². (d) Scheme of plasmonic radiation direction of cube and OD nanostructures placed on MoS₂; FDTD simulation of (i) Au nanocube and (ii) Au OD coupled far-field emission pattern.

nanoparticles are distributed with an interparticle distance of 7–12 nm to empower the gap antenna effect. The nature of hybridization of bilayer MoS₂ with Au plasmonic nanostructures was studied by means of X-ray photoelectron spectroscopy (XPS). The XPS measurements show that there is no chemical interaction between pristine MoS₂ and Au/MoS₂, and the peak shift of the binding energy confirms the synergetic effect and charge transfer between MoS₂ and Au. The corresponding details are discussed in Figure S8 of the Supporting Information. Finally, for measuring the photocurrent of a hybrid plasmonic semiconductor device, finger-type electrodes (Au/Cr) are deposited using a metal mask, as shown in step 5 of Figure 1a. Our strategy of decorating Au nanoparticles onto the as-grown MoS₂ bilayer film enables the transfer-free process of TMDs, which leads to inevitable problems (wrinkles, air bubbles, and crumples), aggravating the device performance.^{38–40} Instead of monolayer MoS₂, we chose the bilayer MoS₂ film considering its lower work function,⁴¹ unique physical properties, broad absorption in visible spectra,²² and stacking orientation-dependent absorption spectra.⁴² Moreover, first-principles calculations demonstrate the higher potential of bilayer MoS₂ for realizing the complete electronic transport property under applied strain.^{43,44} Also, fabrication of bilayer MoS₂ in large scale is more feasible compared to monolayer MoS₂ flakes.

We also conducted Raman measurements for a hybrid plasmonic semiconductor device before electrode deposition to evaluate the strain on bilayer MoS₂ introduced by the hybridized plasmonic structures, as shown in Figure 2a. As per previous investigations, the strain can be correlated with the Raman shift;^{45,46} specifically, the red Raman shift corresponds to tensile strain,⁴⁷ whereas the blue Raman shift accords with

compressive strain.⁴⁸ Therefore, the blue Raman shift shown in Figure 2a demonstrates the compressive strain in this plasmonically engineered MoS₂ bilayer. The weak van der Waals force between two adjacent layers of the MoS₂ bilayer⁴⁹ causes it to undergo compressive strain when an island of Au nanostructures sits on it. Referring to the observed Raman shifts of all nanostructures, the E'2g and A1g modes of MoS₂ hybridized with Au nanocubes show significant shifts of ~2.16 and ~1.83 cm⁻¹, indicating the highest strain. In contrast, the Raman shift of MoS₂ hybridized with Au RD and OD appears very small and the case of Au spheres can be even negligible, indicating much lower strains than the case of Au nanocubes.

This variation of strain stems from different contact interfaces between Au nanostructures and the plain bilayer MoS₂ film. For example, having the large contact area at the interface with the MoS₂ film, Au nanocubes firmly sit on top of the MoS₂ bilayer, thereby providing the highest strain compared to other three complex nanostructures. Previously, the strain-induced band gap shifting behavior of MoS₂ was theoretically predicted by Lu et al. through their first-principles calculations.⁴³ Herein, our results experimentally reveal that the strain inclusion by Au nanostructures causes band gap shifting in the MoS₂ bilayer, evidenced by the blueshift of the PL peak, as shown in Figure 2b. We can monitor that the MoS₂ hybridized with Au nanocubes shows a substantial PL peak shift in contrast to MoS₂ hybridized with other nanostructures as a consequence of the highest strain. This blue shifted PL peak validates the increase in the band gap of MoS₂ due to strain incorporation, whereas the previously reported work of thermally strained bilayer MoS₂ also exhibits a blueshifted band gap.³⁴

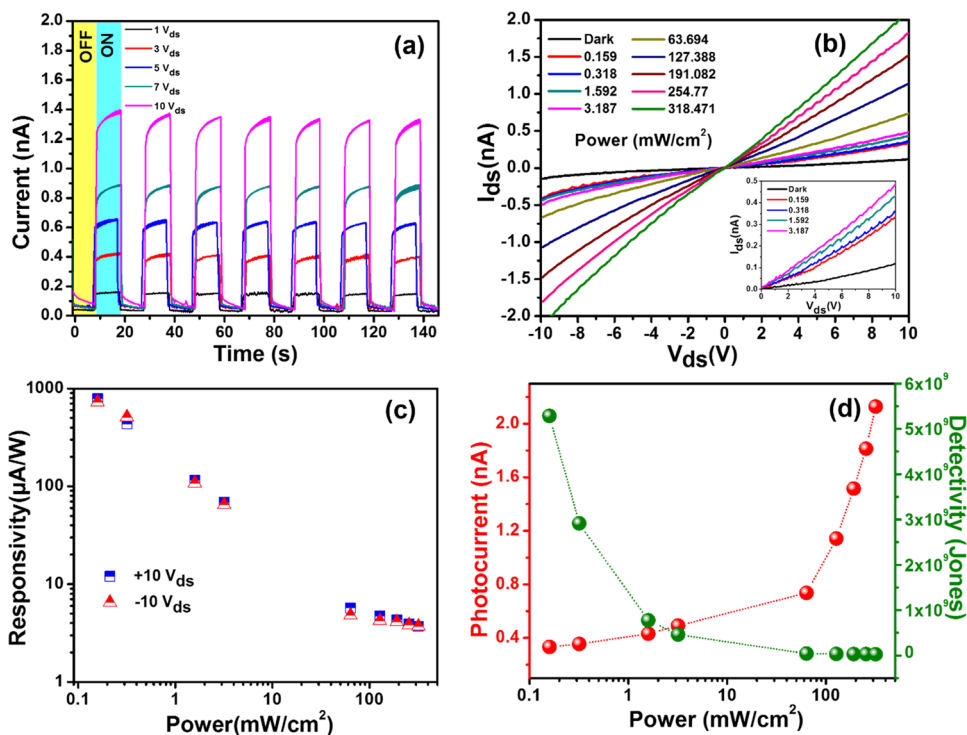


Figure 3. Photoresponse study of CVR-grown bilayer MoS₂ that is decorated with Au nanocubes. (a) Time-dependent photocurrent measurements at various bias voltages ($V_{ds} = 1, 3, 5, 7,$ and 10 V) with a constant laser power density of 318.471 mW/cm². (b) Photoconductivity spectra that are acquired in the dark and with laser illumination at intensities of $0.159, 0.318, 1.592, 3.187, 63.69, 127.38, 191.082, 254.77,$ and 318.471 mW/cm². (c) Plot of photoresponsivity versus laser power intensity at $V_{ds} = +10$ and -10 V. (d) Plot of photocurrent and detectivity versus laser power intensity at $V_{ds} = 10$ V.

In addition to band gap modification, the hybrid Au nanostructures also contribute to substantial photocurrent enhancement in MoS₂ bilayers, as shown in Figure 2c. First, our CVR-grown pristine bilayer MoS₂ shows photocurrent when the laser is on and return to its original state when the laser is off, presenting its semiconducting nature (black curve in Figure 2c). The photocurrent enhancement of the MoS₂ bilayer coupled with four respective Au nanostructures for the fixed drain–source voltage ($V_{ds} = 10$ V) and a power density of 318.471 mW/cm² without gate-induced electric field is displayed in Figure 2c. Obviously, all Au nanostructures contribute to the enhanced photocurrent. When Au with a Fermi level of -5.1 eV and MoS₂ with an electron affinity of 4.29 eV come into contact, a hybrid structure forms with a low Schottky barrier of ~ 0.8 eV.^{50,51} Therefore, the photocurrent enhancement is due to the injection of hot electrons across the Schottky barrier (~ 0.8 eV) at the MoS₂/Au interface. Among four respective Au nanostructures, we distinguish that the MoS₂ bilayer integrated with Au nanocubes shows the highest photocurrent enhancement of 1.4 nA, which is 8 times stronger than that of pristine MoS₂. Again, the consistent reason is that the MoS₂ hybridized with Au nanocubes exhibits the greatest strain-induced band gap modification and benefits more electron transportation across the metal/semiconductor interface by reducing the Schottky barrier height.

Nevertheless, our study reveals that enhancing the quantum yield of MoS₂ is not only from the strain-induced band gap modifications and hot electron injection but also from morphology-dependent emission directionality of plasmonic nanoparticles.⁵² The difference in the radiation patterns of the plasmonic particles has consequences for the coupling of plasmons to MoS₂ placed in their proximity. By observing the

plasmonic effects of various Au morphologies, the Au cube and sphere provide a strong and broad LSPR band across the visible spectrum with a dipolar resonance, whereas RD and OD have complex higher-order plasmonic modes. Comparing the far-field emission patterns of the simple nanocube and the complex OD structure, the coupling of plasmons with MoS₂ is illustrated in Figure 2d. The nanocube has the radiation pattern of the dipolar mode, where most of the energy is radiated along the direction perpendicular to the dipole axis (Figure 2d,i). In contrast, OD has the higher-order mode resonance, where the radiation energy is dispersed in several directions (Figure 2d,ii). Therefore, the highly directional dipolar mode of the nanocube couples more effectively to excitons of MoS₂, outperforming the poorly directional higher-order modes of other complex structures (OD and RD). From all the results aforementioned, including the highest Raman shift and the significant photocurrent enhancement, the Au nanocube possesses the collective advantages of the large strain inclusion in MoS₂ and the efficient coupling from the highly directional dipolar mode to the excitons of MoS₂, thus dramatically augmenting the photoresponse of the MoS₂ bilayer. As a result, we manifest that both the strain-induced band gap modification and the morphology-dependent plasmonic radiation pattern play vital roles in enhancing the photocurrent of the MoS₂ bilayer. A further verification, the finite difference time domain (FDTD)-calculated XY electric field distributions of MoS₂ with interfaces of various Au nanostructures at 520 nm, is also shown in Figure S3 of the Supporting Information.

Since the maximal photocurrent of the MoS₂ bilayer is enhanced by the Au nanocube, profound investigations of its photodetection behavior without gate-induced electric field

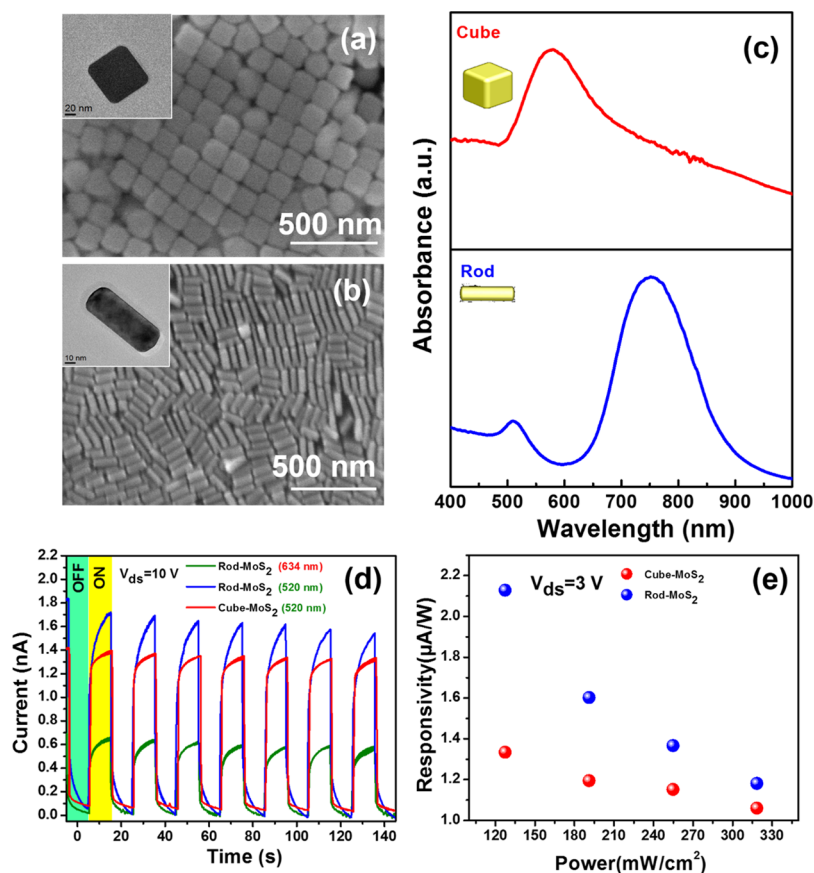


Figure 4. Structural and photodetection characterization of CVR-grown bilayer MoS₂ that is decorated with Au nanorods and nanocubes. SEM images of (a) nanocubes and (b) nanorods (TEM images of individual structures are shown in the figure insets). (c) UV–vis absorption spectra of nanocubes and nanorods. (d) Photocurrent of bilayer MoS₂ that is decorated with nanocubes and nanorods at an applied bias of 10 V and illuminated by 520 and 634 nm laser with a constant power density. (e) Plot of photoresponsivity versus laser power intensity at $V_{ds} = +3$ V for bilayer MoS₂ that is decorated with nanocubes and nanorods.

succeeded, as shown in Figure 3. Photoresponsivity measurements of the hybrid MoS₂ bilayer with Au nanostructures were conducted with finger-type electrodes and an effective illumination area of 169.9 μm^2 . The photoconductivity of the bilayer MoS₂ decorated with Au nanocubes was further studied at various bias voltages ($V_{ds} = 1, 3, 5, 7,$ and 10 V) with a constant power density, as displayed in Figure 3a. We observe an increase in the photocurrent as the applied bias voltage increased. Such a current due to photogenerated carriers (I_{ph}) can be expressed as

$$I_{ph} = 2I_p e \mu \left(\frac{W}{L} \right) V_{ds} \quad (1)$$

where μ denotes the carrier mobility, e is the electronic charge, L and W is the channel length and width of the device, respectively, and I_p is the photocurrent recorded by subtracting the dark current (I_{dark}) from the current when the light is on. In accordance with this equation, we can monitor the photocurrent amplitude as a function of the applied bias voltage (V_{ds}),¹⁷ which is consistent with our result. In addition, photoswitching characteristics were observed by measuring the time-dependent photoresponse with the laser on/off for various bias voltages with a power density of 318.471 mW/cm^2 , therefore revealing the reproducible nature of our device. We measured the photoresponsivity of our hybrid device using a 520 nm diode laser with different intensities of 0.159, 0.318, 1.592, 3.187, 63.69, 127.38, 191.082, 254.77, and 318.471

mW/cm^2 in the dark. Figure 3b exhibits the $I_{ds} - V_{ds}$ plot for dark and laser illumination with various power intensities across -10 to $+10$ V. According to this result, the photocurrent increases gradually as the laser power increases.

Next, we calculated the photoresponsivity of our device, which is a crucial parameter for determining the sensitivity of the photodetector. The photoresponsivity (R_λ) can be expressed as follows

$$R_\lambda = \frac{\Delta I_\lambda}{P_\lambda S} \quad (2)$$

where ΔI_λ denotes the photocurrent, P_λ is the power density, and S is the area of the incident light. Figure 3c presents a plot of the responsivity versus illumination power for two applied bias voltages ($V_{ds} = -10$ V and $+10$ V). This result demonstrates the increasing responsivity with decreasing laser power, which can be correlated with higher laser power, which increases the density of hot carriers and, in turn, enhances the scattering and recombination rate.⁵³ The hybrid semiconductor plasmonic device shows maximum R_λ of up to 790 $\mu\text{A W}^{-1}$ without any gate-induced electric field, which is 6.8 times higher than that of pristine bilayer MoS₂. Further, our plasmonically strained bilayer MoS₂ shows a 32-fold-higher photoresponsivity than previously reported thermally strained bilayer MoS₂ ($R_\lambda = 24.3 \mu\text{A W}^{-1}$), which was grown by the same CVR method.³⁴ Then, we plot the photocurrent and detectivity versus illumination power, as shown in Figure 3d.

We observe the increase in photocurrent as the laser power increases in the log scale, as a consequence of relation $I_{\text{ph}} = \beta P^\alpha$, where P is the incident laser power and α and β are the fitting parameters. However, this linear relation is observed only for power less than 4 mW/cm² and its linearity deviated for power > 50 mW/cm² with another linear slope. The recombination center effects are superlinear in the photocurrent under high-power illumination.^{15,54,55} At high illumination power, the quasi-Fermi levels shift, thereby increasing the carrier lifetime, which, in turn, reduces the recombination rate, thereby resulting in a superlinear behavior of the photocurrent. The comparative performance metrics of already reported plasmonically enhanced MoS₂ photodetectors with our photodetector are tabulated in the Supporting Information (Table S1).

In addition, we calculated the other important parameter of the photodetector, namely, the detectivity (D^*), as shown in Figure 3d. Considering the minimum significance of noise-equivalent power (NEP), the detectivity can be expressed as

$$D^* = (R_{\lambda} \times \sqrt{S}) / \sqrt{2e} I_{\text{dark}} \quad (3)$$

Studies on the detectivity of 2D material-based photodetectors have concluded that detectors that exhibit high photoresponsivity with less dark current have fewer NEPs.^{20,53,56–58} Our hybrid bilayer MoS₂ that is integrated with Au nanostructures possesses a sufficiently low dark current of 0.11864 nA for using eq 3 to calculate the detectivity. The obtained detectivity of our device is $D^* = 5.29 \times 10^9$ J without any gate-induced electric field, which is comparable to that of the back-gated MoS₂ phototransistor ($D^* = 10^{10}$ J).²²

To further study the photogain mechanism and lifetime of traps, we performed time-resolved evolution of our bilayer MoS₂, which was integrated with the plasmonic structure with laser on/off modes for a prolonged time for $V_{\text{ds}} = 10$ V and $P = 318.471$ mW/cm², as shown in Figure S4 of the Supporting Information. We observe a gentle increase in the photocurrent under laser illumination and a sharp drop due to pacific relaxation when the laser is switched off. The rising time of our device is estimated to be 0.26 s and the decay time is 0.45 s. The rising and decay times of our device show significant improvement compared to the Pt strip-enabled MoS₂ bilayer.⁵⁹ In addition, the photoresponsivity measurement of the hybrid MoS₂ bilayer with other Au nanostructures such as Au OD and RD has been carried out, and the results are displayed in Figure S5 of the Supporting Information. The plot of photocurrent versus time for bilayer MoS₂ that is decorated with Au OD and RD at various bias voltages ($V_{\text{ds}} = 1, 3, 5, 7,$ and 10 V) demonstrates the reproducibility and consistent behavior of our hybrid MoS₂/Au device fabricated with the transfer-free process.

In addition, to inspect the photoresponse of MoS₂ due to the aspect ratio-dependent plasmonic mode, we examined the photodetection efficiency of bilayer MoS₂ that is decorated with Au nanocubes and nanorods, as shown in Figure 4. The SEM images of Au nanocubes and nanorods are shown in Figure 4a,b, and the TEM images of individual nanostructures are shown in the figure insets. Figure 4c displays the UV–vis absorption spectra of Au nanocubes with a single plasmon resonance peak and nanorods with longitudinal and transverse resonance peaks. With the Au nanocube being symmetric in structure, the longitudinal and transverse modes of the Au nanocube substantially degenerate, resulting in a ring-like

plasmonic mode (refer to Figure S3a). Meanwhile, the nanorod with a high aspect ratio breaks this degeneracy and creates longitudinal and transverse modes.⁶⁰ The radiation of the longitudinal mode dominates over the transverse mode, as shown in Figure 4c. Figure 4d shows the photocurrent enhancement of the MoS₂ bilayer that is hybridized with Au nanocubes and nanorods and excited at 520 nm at a fixed drain–source voltage ($V_{\text{ds}} = 10$ V) and a power density of 318.471 mW/cm². According to the result, the photocurrent enhancement of hybrid MoS₂/Au nanorods is comparatively higher than that of MoS₂/Au nanocubes. Even though both nanocubes and nanorods exhibit highly directional dipolar modes, being high-aspect-ratio structures, nanorods exhibit higher resonance strength with less radiative plasmon damping compared to low-aspect-ratio nanocubes.⁶¹

Moreover, a previous study on hot electron dynamics reports higher electron injection rates of nanorods. Therefore, with greater resonance strength, less radiation loss, and having highly directional plasmons, nanorods couple more effectively with excitons of MoS₂ than nanocubes. In addition, the higher hot electron injection rate across the Schottky barrier of Au nanorods and MoS₂ stems from the enhanced photocurrent. By observing the photocurrent of bilayer MoS₂ that is hybridized with Au nanorods and excited at wavelengths of 520 and 634 nm, we can understand the photovoltaic effect-dominated photoresponse. Figure 4e reveals the higher photoresponsivity of bilayer MoS₂ that is hybridized with Au nanorods for a fixed applied bias voltage ($V_{\text{ds}} = 3$ V). Plots of the photocurrent versus the illumination power ($V_{\text{ds}} = 3$ V) for MoS₂ that is hybridized with Au nanorods and nanocubes are shown in Figure S6a of the Supporting Information. In addition, the photoresponsivity measurements of the hybrid MoS₂ bilayer that is decorated with Au nanorods and excited at 520 and 634 nm with various bias voltages ($V_{\text{ds}} = 1, 3, 5, 7,$ and 10 V) are shown in Figure S6b,c of the Supporting Information, which again demonstrate the reproducibility of our device.

By taking advantage of the strain-induced band gap modification in bilayer MoS₂ and hot electron injection from plasmonic nanoparticles, substantial enhancement of electron transportation can be achieved, which can be used for electro-optical applications. Recently, theoretical works confirm the reduced Schottky barrier of bilayer MoS₂,⁶² which demonstrates the higher hot electron injection efficiency into bilayer MoS₂. To evaluate the influence of Au on the electronic structure of bilayer MoS₂, we performed first-principles calculations at the density functional theory (DFT) level. DFT calculations were performed by Vienna ab initio simulation package.^{63–65} We used the projector-augmented wave method⁶⁶ as the pseudopotential and Perdew–Burke–Ernzerhof⁶⁷ as the exchange–correlation functional. For combinations of MoS₂ and Au, there were top-site and hole-site structures. Top-site and hole-site structures denote the lowest MoS₂ atoms, which were pointing at the top and hole sites of Au, respectively. We fixed the bottom atom and let those above be relaxed. Each slab had a 10 Å vacuum layer above. We used $15 \times 15 \times 1$ and $19 \times 19 \times 1$ gamma-centered Monkhorst–Pack⁶⁸ k-points in pristine MoS₂'s relaxations and DOS calculations, respectively, whereas $19 \times 19 \times 1$ and $25 \times 25 \times 1$ were used in the relaxations and DOS calculations, respectively, of MoS₂ on Au. Brillouin zone integrations were performed via the tetrahedron method with Blöchl corrections.⁶⁹ The cutoff energy for the plane-wave basis set was 350

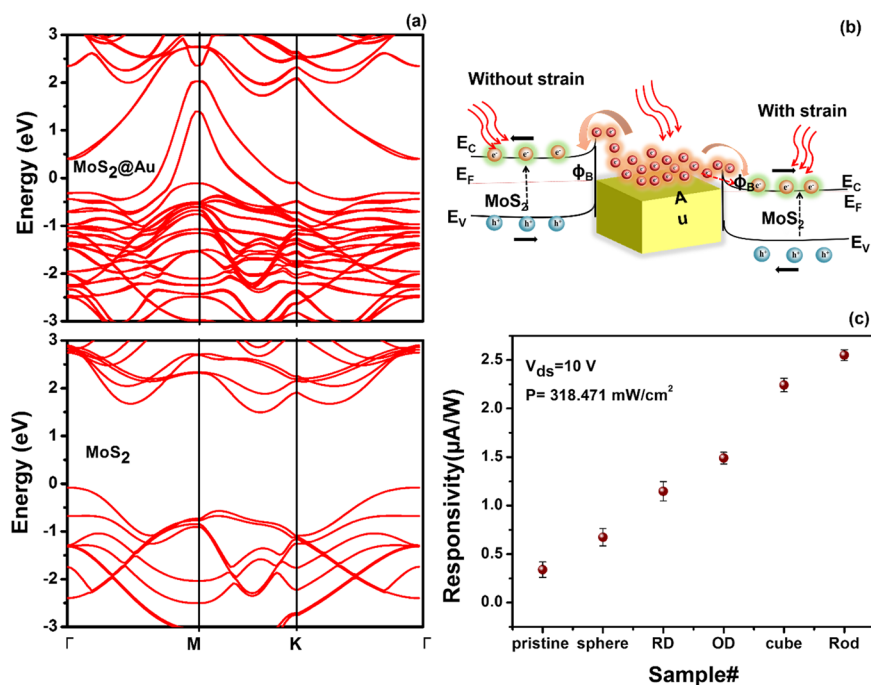


Figure 5. Hot electron injection at the MoS₂/Au interface: (a) Band structure of MoS₂ and Au/MoS₂ calculated by first-principles calculations. (b) Schematic illustration of the mechanism of hot electron injection into strained bilayer MoS₂ from Au. (c) Plot of the photoresponsivity of bilayer MoS₂ with various Au nanostructures at V_{ds} = +10 V with a constant laser power density of 318.471 mW/cm².

eV for all structures. Noncollinear spin–orbit coupling was included for MoS₂ on Au. Figure 5a shows the dramatically modified band structure of MoS₂ by interacting with Au. Faster and easier electron transportation stems up in MoS₂@Au due to the presence of energy states in the band gap regime. Furthermore, Figure S7a of the Supporting Information shows the Fermi level shift of MoS₂ hybridized with Au toward the conduction band with a new isolated energy level that is formed in the band gap, thereby reducing the interfacial Schottky barrier between Au and MoS₂.⁷⁰

To gain more insight into the exciton and plasmon coupling, time-resolved photoluminescence (TR-PL) measurements have been carried out for MoS₂ and MoS₂ decorated with Au nanoparticles, as shown in Figure S7b of the Supporting Information. The PL decay time of as-grown MoS₂ is 4.483 ns, but it shortens to 3.183 ns when MoS₂ was decorated with Au nanoparticles. This shortened decay time results from the charge transfer between Au and MoS₂.⁷¹ To understand the influence of the electron migration behavior on the localized strain that comes from the Au nanostructures that are decorated on bilayer MoS₂, two band gap regions on the same 2D material have been proposed, as shown in Figure 5b. In our device, the bilayer MoS₂ region under the Au nanoparticles has a distinct strain compared to the region without Au nanoparticles. Therefore, the localized strain on our bilayer MoS₂ is not uniform. Hence, we predict the two distinct band gap regions, with and without strain. Normally, in the strain-free region, when Au and MoS₂ come into contact, the Schottky barrier at the interface is formed after the Fermi alignment. Upon light irradiation, the hot electrons can overcome this barrier and enter the conduction band of MoS₂. Meanwhile, the region with strain acquires band gap modification, which can facilitate easy hot electron injection. Figure 5c shows the tunable photoresponsivity of CVR-grown bilayer MoS₂ via judicious selection of plasmonic nanoparticle

morphology. Therefore, our work reveals the manipulation of the optoelectronic behavior of bilayer MoS₂ by plasmonic nanoparticles, which depends on the emission pattern of plasmonic particles, strain-induced band gap modification, and hot electron injection efficiency across the Schottky barrier.

In conclusion, we demonstrated superior photodetection of bilayer MoS₂ by hybridizing it with a variety of morphology-controlled plasmonic nanoparticles, nanocubes, octahedra, rhombic dodecahedra, and nanospheres. Among these hybrids, the bilayer MoS₂ decorated with Au nanocubes undergoes the highest strain, thereby leading to a blueshifted band gap. Such a modified band structure in the MoS₂-Au hybrid was confirmed by both Raman and PL measurements and manifested by the first-principles calculations. Meanwhile, based on the photocurrent measurements, we also observed distinct photocurrent enhancements in the MoS₂ bilayer that was integrated with various morphology-controlled Au nanostructures. In addition, we scrutinized the photodetection behavior of MoS₂ that is hybridized with Au nanocubes and obtained large photogain and a maximum photoresponsivity of 790 μA W⁻¹ without any gate-induced electric field. This experimental result is 32-fold-higher than that of the previously reported thermally strained bilayer MoS₂ (R_λ = 24.3 μA W⁻¹), grown by same CVR method. Although hot electron injection was a substantial factor for photocurrent enhancement in hybrid plasmonic semiconductor devices, our investigations further indicate that the highly directional plasmonic modes, high-aspect-ratio plasmonic nanostructures with less damping loss, and plasmonic strain-induced beneficial band structure modifications were the key parameters for efficient outcomes. As a consequence, our study opens up new approaches for designing highly tailorable plasmonic nanoparticle-integrated transition-metal dichalcogenide-based optoelectronic devices.

■ EXPERIMENTAL METHODS

Fabrication of Bilayer Molybdenum Disulfide (MoS₂) by a Two-Step Process. The precursor molybdenum oxide (MoO₃) film of 2 nm in thickness was deposited at 0.1 Å/s using an E-gun evaporator. The sulfur source was placed upstream of the gas, and the deposited MoO₃ sapphire substrate was placed in the heating zone of the furnace tube. To completely cover the sulfur powder, heating tape was wrapped around the quartz tube. Then, a pressure of approximately 550 torr with a H₂/N₂ (75%/25%) gas mixture that was flowing at 50 sccm was maintained during sulfurization. After the heating tape and furnace reached temperatures of approximately 180 and 1000 °C, respectively, MoO₃, hydrogen, and sulfur vapor reacted with one another, eventually synthesizing MoS₂ on the sapphire substrate.

Synthesis of Au Nanostructures. Octahedral Nanostructures. The hydrothermal synthesis of octahedral gold nanocrystals was performed according to a previous work.⁷² For the reaction, 9.7 mL of ultrahigh-purity water, 0.055 g of CTAB, 250 μL of 0.01 M HAuCl₄, and 50 μL of 0.1 M trisodium citrate were added to a glass vial with a Teflon-lined polypropylene cap. Once the oven temperature reached 110 °C, sample vials were loaded into the oven and heated for 24 hr. To remove the residual CTAB surfactant, the solutions were centrifuged twice at 6000 rpm for 20 min. Finally, the nanocrystals were stored in deionized water.

Cubic and Rhombic Dodecahedral Nanostructures. Cubic and rhombic dodecahedral nanostructures were synthesized using seed-mediated growth according to a previously reported work.⁷³ A seed solution was prepared with a volume of 10 mL of aqueous solution that contained 2.5 × 10⁻⁴ M HAuCl₄ and 0.10 M CTAC. Meanwhile, 10 mL of a 0.02 M ice-cold NaBH₄ solution was made. Then, 0.45 mL of the NaBH₄ solution was added to the HAuCl₄ solution with stirring. The resulting solution turned brown immediately, thereby indicating the formation of gold particles. The seed solution was aged for 1 h at 30 °C to decompose excess borohydride. The growth solution was prepared in two vials, which were labeled A and B. First, 0.32 g of CTAC surfactant was added. Depending on the morphology of the gold nanocrystals to be synthesized, slightly different volumes of deionized water were added to each vial: 9.625 mL for cubic and 9.565 mL for RD. The vials were kept in a water bath at 30 °C. To both vials, 250 μL of a 0.01 M HAuCl₄ solution and 10 μL of 0.01 M NaBr were added. Finally, for the synthesis of gold nanocubes, 90 μL of ascorbic acid was used, whereas 150 μL of ascorbic acid was added for the growth of rhombic dodecahedra. The total solution volume in each vial was 10 mL. Next, 25 μL of the seed solution was added to the solution in vial A with shaking until the solution color turned light pink (~5 s). After that, 25 μL of the solution in vial A was transferred to vial B with thorough mixing for ~10 s. The solution in vial B was left undisturbed for 15 min for particle growth and centrifuged at 3000 rpm for 10 min.

Nanorods. The Au nanorods were prepared by following a previously reported study.⁷⁴ For the seed solution, 0.250 mL of an aqueous 0.01 M solution of HAuCl₄·3H₂O was added to 7.5 mL of a 0.10 M CTAB solution in a glass vial. The solution appeared bright brown-yellow in color. Then, 0.600 mL of an aqueous 0.01 M ice-cold NaBH₄ solution was added all at once, followed by rapid shaking. The solution developed a pale brown-yellow color. Then, the test tube was kept in a water bath that was maintained at 25 °C for future use. For the growth solution, 4.75 mL of 0.10 M CTAB, 0.200 mL of 0.01 M HAuCl₄·3H₂O, and 0.030 mL of 0.01 M AgNO₃ solutions were added with gentle mixing. The solution at this stage appeared bright brown-yellow in color. Then, 0.032 mL of 0.10 M ascorbic acid (AA) was added to it. The solution became colorless upon mixing of AA. Then, 0.010 mL of seed solution was added, and the reaction mixture was gently mixed for 10 s and left undisturbed for at least 20 h. Finally, the nanorods were centrifuged and stored in deionized water.

Characterization. To confirm the morphology and dimensions of the Au nanostructures, SEM was performed using a Hitachi S-8010 FESEM. The Raman and PL enhancement studies were carried out via micro-Raman spectroscopy (HORIBA, LabRAM, HR800) using

laser excitation with a wavelength of 514 nm. The bilayer MoS₂ was transferred onto the TEM grid, and successful bilayer fabrication was confirmed by HR-TEM images using a JEOL JEM-3000F. The electrical characteristics were measured using a conventional probe station system (2400 and 420, Keithley). To measure the photocurrent, 520 and 634 nm laser excitation sources were utilized. Time-dependent photocurrent measurements were performed using a homemade laser shutter system.

■ ASSOCIATED CONTENT

Supporting Information

The Supporting Information is available free of charge at <https://pubs.acs.org/doi/10.1021/acs.chemmater.9b02886>.

Raman spectrum of bilayer MoS₂ on a sapphire substrate; UV-vis absorption spectra of various nanostructures; size distribution histogram plot of Au nanostructures; FDTD simulated XY field distribution of bilayer MoS₂ interfaces with various Au nanostructures; prolonged time-resolved photoresponse performance of the hybrid device; time-dependent photocurrent measurements of bilayer MoS₂ that is decorated with Au OD, RD, and nanorods at various bias voltages ($V_{ds} = 1, 3, 5, 7, \text{ and } 10 \text{ V}$); plot of photocurrent versus laser power intensity at $V_{ds} = 3 \text{ V}$ for bilayer MoS₂ that is decorated with Au nanocubes and nanorods; partial density of states of MoS₂ and Au/MoS₂ hybrid by first-principles calculations; time-resolved photoluminescence spectra of MoS₂ and Au/MoS₂; X-ray photoelectron spectroscopy study for MoS₂ hybridized with Au; and performance metrics of plasmon-enhanced MoS₂ photodetectors (PDF)

■ AUTHOR INFORMATION

Corresponding Author

Ta-Jen Yen – Department of Materials Science and Engineering, National Tsing Hua University, Hsinchu 30013, Taiwan, R.O.C.; orcid.org/0000-0003-3613-699X; Email: tjyen@mx.nthu.edu.tw

Authors

Pavithra Sriram – Department of Materials Science and Engineering, National Tsing Hua University, Hsinchu 30013, Taiwan, R.O.C.

Yu-Po Wen – Department of Materials Science and Engineering, National Tsing Hua University, Hsinchu 30013, Taiwan, R.O.C.

Arumugam Manikandan – Department of Materials Science and Engineering, National Tsing Hua University, Hsinchu 30013, Taiwan, R.O.C.; orcid.org/0000-0001-7284-2002

Kun-Chieh Hsu – Department of Physics, National Tsing Hua University, Hsinchu 30013, Taiwan, R.O.C.

Shin-Yi Tang – Department of Materials Science and Engineering, National Tsing Hua University, Hsinchu 30013, Taiwan, R.O.C.

Bo-Wei Hsu – Department of Materials Science and Engineering, National Tsing Hua University, Hsinchu 30013, Taiwan, R.O.C.

Yu-Ze Chen – Department of Materials Science and Engineering, National Tsing Hua University, Hsinchu 30013, Taiwan, R.O.C.

Hao-Wu Lin – Department of Materials Science and Engineering, National Tsing Hua University, Hsinchu 30013, Taiwan, R.O.C.; orcid.org/0000-0003-4216-7995

Hornng-Tay Jeng – Department of Physics, National Tsing Hua University, Hsinchu 30013, Taiwan, R.O.C.; orcid.org/0000-0002-2881-3826

Yu-Lun Chueh – Department of Materials Science and Engineering, National Tsing Hua University, Hsinchu 30013, Taiwan, R.O.C.; orcid.org/0000-0002-0155-9987

Complete contact information is available at:

<https://pubs.acs.org/10.1021/acs.chemmater.9b02886>

Notes

The authors declare no competing financial interest.

ACKNOWLEDGMENTS

This project is financially supported by the Ministry of Science and Technology (MOST 106-2221-E-007-038-MY3, 107-2221-E-007-016-MY3, 107-2923-E-007-006-MY2, and 108-3017-E-007-002), and also by the “High Entropy Materials Center” from The Featured Areas Research Center Program within the framework of the Higher Education Sprout Project by the Ministry of Education (MOE) in Taiwan (108QR001J4).

REFERENCES

- (1) Wang, Q. H.; Kalantar-Zadeh, K.; Kis, A.; Coleman, J. N.; Strano, M. S. Electronics and optoelectronics of two-dimensional transition metal dichalcogenides. *Nat. Nanotechnol.* **2012**, *7*, 699.
- (2) Dai, J.; Zeng, X. C. Bilayer phosphorene: effect of stacking order on bandgap and its potential applications in thin-film solar cells. *J. phys. Chem. Lett.* **2014**, *5*, 1289–1293.
- (3) Radisavljevic, B.; Radenovic, A.; Brivio, J.; Giacometti, V.; Kis, A. Single-layer MoS₂ transistors. *Nat. Nanotechnol.* **2011**, *6*, 147.
- (4) Yan, J.; Kim, M.-H.; Elle, J. A.; Sushkov, A. B.; Jenkins, G. S.; Milchberg, H. M.; Fuhrer, M. S.; Drew, H. D. Dual-gated bilayer graphene hot-electron bolometer. *Nat. Nanotechnol.* **2012**, *7*, 472.
- (5) Vicarelli, L.; Vitiello, M. S.; Coquillat, D.; Lombardo, A.; Ferrari, A. C.; Knap, W.; Polini, M.; Pellegrini, V.; Tredicucci, A. Graphene field-effect transistors as room-temperature terahertz detectors. *Nat. Mater.* **2012**, *11*, 865.
- (6) Pospischil, A.; Humer, M.; Furchi, M. M.; Bachmann, D.; Guider, R.; Fromherz, T.; Mueller, T. CMOS-compatible graphene photodetector covering all optical communication bands. *Nat. Photonics* **2013**, *7*, 892.
- (7) Mueller, T.; Xia, F.; Avouris, P. Graphene photodetectors for high-speed optical communications. *Nat. Photonics* **2010**, *4*, 297.
- (8) Baugher, B. W. H.; Churchill, H. O. H.; Yang, Y.; Jarillo-Herrero, P. Optoelectronic devices based on electrically tunable p–n diodes in a monolayer dichalcogenide. *Nat. Nanotechnol.* **2014**, *9*, 262.
- (9) Pospischil, A.; Furchi, M. M.; Mueller, T. Solar-energy conversion and light emission in an atomic monolayer p–n diode. *Nat. Nanotechnol.* **2014**, *9*, 257–261.
- (10) Perea-López, N.; Elias, A. L.; Berkdemir, A.; Castro-Beltrán, A.; Gutiérrez, H. R.; Feng, S.; Lv, R.; Hayashi, T.; López-Urías, F.; Ghosh, S.; Muchharla, B.; Talapatra, S.; Terrones, H.; Terrones, M. Photosensor device based on few-layered WS₂ films. *Adv. Funct. Mater.* **2013**, *23*, 5511–5517.
- (11) Buscema, M.; Barkelid, M.; Zwiller, V.; van der Zant, H. S. J.; Steele, G. A.; Castellanos-Gomez, A. Large and tunable photothermoelectric effect in single-layer MoS₂. *Nano Lett.* **2013**, *13*, 358–363.
- (12) Fontana, M.; Deppe, T.; Boyd, A. K.; Rinzan, M.; Liu, A. Y.; Paranjape, M.; Barbara, P. Electron-hole transport and photovoltaic effect in gated MoS₂ Schottky junctions. *Sci. Rep.* **2013**, *3*, 1634.
- (13) Wu, C.-C.; Jariwala, D.; Sangwan, V. K.; Marks, T. J.; Hersam, M. C.; Lauhon, L. J. Elucidating the photoresponse of ultrathin MoS₂ field-effect transistors by scanning photocurrent microscopy. *J. Phys. Chem. Lett.* **2013**, *4*, 2508–2513.
- (14) Lin, J.; Li, H.; Zhang, H.; Chen, W. Plasmonic enhancement of photocurrent in MoS₂ field-effect-transistor. *Appl. Phys. Lett.* **2013**, *102*, 203109.
- (15) Tsai, D.-S.; Liu, K.-K.; Lien, D.-H.; Tsai, M.-L.; Kang, C.-F.; Lin, C.-A.; Li, L.-J.; He, J.-H. Few-layer MoS₂ with high broadband photogain and fast optical switching for use in harsh environments. *ACS Nano* **2013**, *7*, 3905–3911.
- (16) Zhang, W.; Huang, J. K.; Chen, C. H.; Chang, Y. H.; Cheng, Y. J.; Li, L. J. High-gain phototransistors based on a CVD MoS₂ monolayer. *Adv. Mater.* **2013**, *25*, 3456–3461.
- (17) Lopez-Sanchez, O.; Lembke, D.; Kayci, M.; Radenovic, A.; Kis, A. Ultrasensitive photodetectors based on monolayer MoS₂. *Nat. Nanotechnol.* **2013**, *8*, 497.
- (18) Lee, H. S.; Min, S.-W.; Chang, Y.-G.; Park, M. K.; Nam, T.; Kim, H.; Kim, J. H.; Ryu, S.; Im, S. MoS₂ nanosheet phototransistors with thickness-modulated optical energy gap. *Nano Lett.* **2012**, *12*, 3695–3700.
- (19) Britnell, L.; Ribeiro, R. M.; Eckmann, A.; Jalil, R.; Belle, B. D.; Mishchenko, A.; Kim, Y.-J.; Gorbachev, R. V.; Georgiou, T.; Morozov, S. V.; Grigorenko, A. N.; Geim, A. K.; Casiraghi, C.; Castro Neto, A. H. C.; Novoselov, K. S. Strong light-matter interactions in heterostructures of atomically thin films. *Science* **2013**, *340*, 1311–1314.
- (20) Jacobs-Gedrim, R. B.; Shanmugam, M.; Jain, N.; Durcan, C. A.; Murphy, M. T.; Murray, T. M.; Matyi, R. J.; Moore, R. L., II; Yu, B. Extraordinary photoresponse in two-dimensional In₂Se₃ nanosheets. *ACS Nano* **2014**, *8*, 514–521.
- (21) Yin, Z.; Li, H.; Li, H.; Jiang, L.; Shi, Y.; Sun, Y.; Lu, G.; Zhang, Q.; Chen, X.; Zhang, H. Single-layer MoS₂ phototransistors. *ACS Nano* **2012**, *6*, 74–80.
- (22) Choi, W.; Cho, M. Y.; Konar, A.; Lee, J. H.; Cha, G.-B.; Hong, S. C.; Kim, S.; Kim, J.; Jena, D.; Joo, J.; Kim, S. High-detectivity multilayer MoS₂ phototransistors with spectral response from ultraviolet to infrared. *Adv. Mater.* **2012**, *24*, 5832–5836.
- (23) Mak, K. F.; Lee, C.; Hone, J.; Shan, J.; Heinz, T. F. Atomically thin MoS₂: a new direct-gap semiconductor. *Phys. Rev. Lett.* **2010**, *105*, 136805.
- (24) Salehzadeh, O.; Tran, N. H.; Liu, X.; Shih, I.; Mi, Z. Exciton kinetics, quantum efficiency, and efficiency droop of monolayer MoS₂ light-emitting devices. *Nano Lett.* **2014**, *14*, 4125–4130.
- (25) Kumarasinghe, C. S.; Premaratne, M.; Bao, Q.; Agrawal, G. P. Theoretical analysis of hot electron dynamics in nanorods. *Sci. Rep.* **2015**, *5*, 12140.
- (26) Li, X.; Zhu, J.; Wei, B. Hybrid nanostructures of metal/two-dimensional nanomaterials for plasmon-enhanced applications. *Chem. Soc. Rev.* **2016**, *45*, 3145–3187.
- (27) Chen, M.; Shao, L.; Kershaw, S. V.; Yu, H.; Wang, J.; Rogach, A. L.; Zhao, N. Photocurrent enhancement of HgTe quantum dot photodiodes by plasmonic gold nanorod structures. *ACS Nano* **2014**, *8*, 8208–8216.
- (28) Tame, M. S.; McEney, K. R.; Özdemir, Ş. K.; Lee, J.; Maier, S. A.; Kim, M. S. Quantum plasmonics. *Nat. Phys.* **2013**, *9*, 329.
- (29) Ghatak, S.; Pal, A. N.; Ghosh, A. Nature of electronic states in atomically thin MoS₂ field-effect transistors. *ACS Nano* **2011**, *5*, 7707–7712.
- (30) Yan, J.; Ma, C.; Liu, P.; Yang, G. Plasmon-Induced Energy Transfer and Photoluminescence Manipulation in MoS₂ with a Different Number of Layers. *ACS Photonics* **2017**, *4*, 1092–1100.
- (31) Gao, W.; Lee, Y. H.; Jiang, R.; Wang, J.; Liu, T.; Ling, X. Y. Localized and continuous tuning of monolayer MoS₂ photoluminescence using a single shape-controlled Ag nanoantenna. *Adv. Mater.* **2016**, *28*, 701–706.
- (32) Shi, Y.; Wang, J.; Wang, C.; Zhai, T. T.; Bao, W. J.; Xu, J. J.; Xia, X. H.; Chen, H. Y. Hot electron of Au nanorods activates the electrocatalysis of hydrogen evolution on MoS₂ nanosheets. *J. Am. Chem. Soc.* **2015**, *137*, 7365–7370.
- (33) Sriram, P.; Su, D. S.; Periasamy, A. P.; Manikandan, A.; Wang, S. W.; Chang, H. T.; Chueh, Y. L.; Yen, T. J. Hybridizing Strong Quadrupole Gap Plasmons Using Optimized Nanoantennas with

Bilayer MoS₂ for Excellent Photo-Electrochemical Hydrogen Evolution. *Adv. Energy Mater.* **2018**, *8*, 1801184.

(34) Wang, S.-W.; Medina, H.; Hong, K.-B.; Wu, C.-C.; Qu, Y.; Manikandan, A.; Su, T.-Y.; Lee, P.-T.; Huang, Z.-Q.; Wang, Z.; Chuang, F.-C.; Kuo, H.-C.; Chueh, Y.-L. Thermally Strained Band Gap Engineering of Transition-Metal Dichalcogenide Bilayers with Enhanced Light–Matter Interaction toward Excellent Photodetectors. *ACS Nano* **2017**, *11*, 8768–8776.

(35) Najmaei, S.; Liu, Z.; Zhou, W.; Zou, X.; Shi, G.; Lei, S.; Yakobson, B. I.; Idrobo, J. C.; Ajayan, P. M.; Lou, J. Vapour phase growth and grain boundary structure of molybdenum disulphide atomic layers. *Nat. Mater.* **2013**, *12*, 754–759.

(36) Park, J.; Choudhary, N.; Smith, J.; Lee, G.; Kim, M.; Choi, W. Thickness modulated MoS₂ grown by chemical vapor deposition for transparent and flexible electronic devices. *Appl. Phys. Lett.* **2015**, *106*, No. 012104.

(37) Tao, J.; Chai, J.; Lu, X.; Wong, L. M.; Wong, T. I.; Pan, J.; Xiong, Q.; Chi, D.; Wang, S. Growth of wafer-scale MoS₂ monolayer by magnetron sputtering. *Nanoscale* **2015**, *7*, 2497–2503.

(38) Reserbat-Plantey, A.; Kalita, D.; Han, Z.; Ferlazzo, L.; Autier-Laurent, S.; Komatsu, K.; Li, C.; Weil, R.; Ralko, A.; Marty, L.; Guéron, S.; Bendiab, N.; Bouchiat, H.; Bouchiat, V. Strain superlattices and macroscale suspension of graphene induced by corrugated substrates. *Nano Lett.* **2014**, *14*, 5044–5051.

(39) Vejpravova, J.; Pacakova, B.; Endres, J.; Mantlikova, A.; Verhagen, T.; Vales, V.; Frank, O.; Kalbac, M. Graphene wrinkling induced by monodisperse nanoparticles: facile control and quantification. *Sci. Rep.* **2015**, *5*, 15061.

(40) Tomori, H.; Kanda, A.; Goto, H.; Ootuka, Y.; Tsukagoshi, K.; Moriyama, S.; Watanabe, E.; Tsuya, D. Introducing nonuniform strain to graphene using dielectric nanopillars. *Appl. Phys. Express* **2011**, *4*, No. 075102.

(41) Hao, S.; Yang, B.; Gao, Y. Controllable growth and electrostatic properties of Bernal stacked bilayer MoS₂. *J. Appl. Phys.* **2016**, *120*, 124310.

(42) Park, S.; Kim, H.; Kim, M. S.; Han, G. H.; Kim, J. Dependence of Raman and absorption spectra of stacked bilayer MoS₂ on the stacking orientation. *Opt. Express* **2016**, *24*, 21551–21559.

(43) Lu, P.; Wu, X.; Guo, W.; Zeng, X. C. Strain-dependent electronic and magnetic properties of MoS₂ monolayer, bilayer, nanoribbons and nanotubes. *Phys. Chem. Chem. Phys.* **2012**, *14*, 13035–13040.

(44) Bhattacharyya, S.; Pandey, T.; Singh, A. K. Effect of strain on electronic and thermoelectric properties of few layers to bulk MoS₂. *Nanotechnology* **2014**, *25*, 465701.

(45) Desai, S. B.; Seol, G.; Kang, J. S.; Fang, H.; Battaglia, C.; Kapadia, R.; Ager, J. W.; Guo, J.; Javey, A. Strain-induced indirect to direct bandgap transition in multilayer WSe₂. *Nano Lett.* **2014**, *14*, 4592–4597.

(46) Yang, L.; Cui, X.; Zhang, J.; Wang, K.; Shen, M.; Zeng, S.; Dayeh, S. A.; Feng, L.; Xiang, B. Lattice strain effects on the optical properties of MoS₂ nanosheets. *Sci. Rep.* **2014**, *4*, 5649.

(47) Conley, H. J.; Wang, B.; Ziegler, J. I.; Haglund, R. F., Jr.; Pantelides, S. T.; Bolotin, K. I. Bandgap engineering of strained monolayer and bilayer MoS₂. *Nano Lett.* **2013**, *13*, 3626–3630.

(48) Hui, Y. Y.; Liu, X.; Jie, W.; Chan, N. Y.; Hao, J.; Hsu, Y. T.; Li, L. J.; Guo, W.; Lau, S. P. Exceptional tunability of band energy in a compressively strained trilayer MoS₂ sheet. *ACS Nano* **2013**, *7*, 7126–7131.

(49) Ghosh, P. N.; Maiti, C. R. Interlayer force and Davydov splitting in 2H–MoS₂. *Phys. Rev. B* **1983**, *28*, 2237.

(50) Yu, C.-H.; Su, P.; Chuang, C.-T. Impact of Random Variations on Cell Stability and Write-Ability of Low-Voltage SRAMs Using Monolayer and Bilayer Transition Metal Dichalcogenide (TMD) MOSFETs. *IEEE Electron Device Lett.* **2016**, *37*, 928–931.

(51) Zhang, P.; Fujitsuka, M.; Majima, T. Hot electron-driven hydrogen evolution using anisotropic gold nanostructure assembled monolayer MoS₂. *Nanoscale* **2017**, *9*, 1520–1526.

(52) Biagioni, P.; Huang, J.-S.; Hecht, B. Nanoantennas for visible and infrared radiation. *Rep. Prog. Phys.* **2012**, *75*, No. 024402.

(53) Su, G.; Hadjiev, V. G.; Loya, P. E.; Zhang, J.; Lei, S.; Maharjan, S.; Dong, P.; Ajayan, P. M.; Lou, J.; Peng, H. Chemical vapor deposition of thin crystals of layered semiconductor SnS₂ for fast photodetection application. *Nano Lett.* **2015**, *15*, 506–513.

(54) Bao, Q.; Loh, K. P. Graphene photonics, plasmonics, and broadband optoelectronic devices. *ACS Nano* **2012**, *6*, 3677–3694.

(55) Hu, P.; Wen, Z.; Wang, L.; Tan, P.; Xiao, K. Synthesis of few-layer GaSe nanosheets for high performance photodetectors. *ACS Nano* **2012**, *6*, 5988–5994.

(56) Ulaganathan, R. K.; Lu, Y. Y.; Kuo, C. J.; Tamalampudi, S. R.; Sankar, R.; Boopathi, K. M.; Anand, A.; Yadav, K.; Mathew, R. J.; Liu, C. R.; Chou, F. C.; Chen, Y. T. High photosensitivity and broad spectral response of multi-layered germanium sulfide transistors. *Nanoscale* **2016**, *8*, 2284–2292.

(57) Buscema, M.; Island, J. O.; Groenendijk, D. J.; Blanter, S. I.; Steele, G. A.; van der Zant, H. S. J.; Castellanos-Gomez, A. Photocurrent generation with two-dimensional van der Waals semiconductors. *Chem. Soc. Rev.* **2015**, *44*, 3691–3718.

(58) Hu, P.; Wang, L.; Yoon, M.; Zhang, J.; Feng, W.; Wang, X.; Wen, Z.; Idrobo, J. C.; Miyamoto, Y.; Geohagan, D. B.; Xiao, K. Highly responsive ultrathin GaS nanosheet photodetectors on rigid and flexible substrates. *Nano Lett.* **2013**, *13*, 1649–1654.

(59) Kumar, R.; Sharma, A.; Kaur, M.; Husale, S. Pt-Nanostrip-enabled plasmonically enhanced broad spectral photodetection in bilayer MoS₂. *Adv. Opt. Mater.* **2017**, *5*, 1700009.

(60) Knight, M. W.; Liu, L.; Wang, Y.; Brown, L.; Mukherjee, S.; King, N. S.; Everitt, H. O.; Nordlander, P.; Halas, N. J. Aluminum plasmonic nanoantennas. *Nano Lett.* **2012**, *12*, 6000–6004.

(61) Fernández-García, R.; Sonnefraud, Y.; Fernández-Domínguez, A. I.; Giannini, V.; Maier, S. A. Design considerations for near-field enhancement in optical antennas. *Contemp. Phys.* **2014**, *55*, 1–11.

(62) Zhong, H.; Quhe, R.; Wang, Y.; Ni, Z.; Ye, M.; Song, Z.; Pan, Y.; Yang, J.; Yang, L.; Lei, M.; Shi, J.; Lu, J. Interfacial properties of monolayer and bilayer MoS₂ contacts with metals: beyond the energy band calculations. *Sci. Rep.* **2016**, *6*, 21786.

(63) Kresse, G.; Hafner, J. Ab initio molecular dynamics for liquid metals. *Phys. Rev. B* **1993**, *47*, 558–561.

(64) Kresse, G.; Furthmüller, J.; Hafner, J. Theory of the crystal structures of selenium and tellurium: the effect of generalized-gradient corrections to the local-density approximation. *Phys. Rev. B* **1994**, *50*, 13181.

(65) Kresse, G.; Furthmüller, J. Efficiency of ab-initio total energy calculations for metals and semiconductors using a plane-wave basis set. *Comput. Mater. Sci.* **1996**, *6*, 15–50.

(66) Blöchl, P. E. Projector augmented-wave method. *Phys. Rev. B* **1994**, *50*, 17953.

(67) Perdew, J. P.; Burke, K.; Ernzerhof, M. Generalized gradient approximation made simple. *Phys. Rev. Lett.* **1996**, *77*, 3865.

(68) Monkhorst, H. J.; Pack, J. D. Special points for Brillouin-zone integrations. *Phys. Rev. B* **1976**, *13*, 5188.

(69) Blöchl, P. E.; Jepsen, O.; Andersen, O. K. Improved tetrahedron method for Brillouin-zone integrations. *Phys. Rev. B* **1994**, *49*, 16223–16233.

(70) Cheng, W.; Su, H.; Tang, F.; Che, W.; Huang, Y.; Zheng, X.; Yao, T.; Liu, J.; Hu, F.; Jiang, Y.; Liu, Q.; Wei, S. Synergetic enhancement of plasmonic hot-electron injection in Au cluster-nanoparticle/C₃N₄ for photocatalytic hydrogen evolution. *J. Mater. Chem.* **2017**, *5*, 19649–19655.

(71) Pan, J.; Chen, J.; Zhao, D.; Huang, Q.; Khan, Q.; Liu, X.; Tao, Z.; Zhang, Z.; Lei, W. Surface plasmon-enhanced quantum dot light-emitting diodes by incorporating gold nanoparticles. *Opt. Express* **2016**, *24*, A33–A43.

(72) Chang, C.-C.; Wu, H.-L.; Kuo, C.-H.; Huang, M. H. Hydrothermal synthesis of monodispersed octahedral gold nanocrystals with five different size ranges and their self-assembled structures. *Chem. Mater.* **2008**, *20*, 7570–7574.

(73) Wu, H. L.; Kuo, C. H.; Huang, M. H. Seed-mediated synthesis of gold nanocrystals with systematic shape evolution from cubic to trisoctahedral and rhombic dodecahedral structures. *Langmuir* **2010**, *26*, 12307–12313.

(74) Sau, T. K.; Murphy, C. J. Seeded high yield synthesis of short Au nanorods in aqueous solution. *Langmuir* **2004**, *20*, 6414–6420.